Desalination and Water Treatment
www.deswater.com

doi:10.5004/dwt.2018.22471

116 (2018) 1–18
June

An experimentally calibrated model for heat and mass transfer in full-scale direct contact membrane distillation

Emad Ali[a,*], Jamel Orfi[b]

[a]*Chemical Engineering Department, King Saud University, Riyadh11421, Saudi Arabia, email: amkamal@ksu.edu.sa (E. Ali)*
[b]*Mechanical Engineering Department, King Saud University, Riyadh11421, Saudi Arabia*

Received 7 November 2017; Accepted 6 May 2018

ABSTRACT

This paper presents experimental and theoretical results for the performance of direct contact membrane distillation (DCMD). An experimental DCMD unit is used to study the thermal and material behavior of the closed-loop system, investigating the effect of feed flow rate, inlet temperature, and salinity. The results indicate the proportional growth of water production with increasing feed flow rate and inlet temperature. Specifically, the mass flux increases from 0.6 to 1.7 kg/(m²·h) when the inlet temperature rises from 50 to 80°C at 300 L/h feed flow rate. Similarly, the mass flux increases from 0.27 to 1.7kg/(m²·h) when the feed flow rate increases from 50 to 300 L/h at an inlet temperature of 80°C. A transition region is observed at a feed flow rate of 100 L/h; at higher flow rates, the heat flux saturates causing the exit permeate temperature and recovery ratio to reach saturation. Solution salinity moderately affects the mass flux but only slightly affects the heat flux. A theoretical model based on heat and mass transfer balances is developed, and careful adjustment of the mass transfer coefficient and heat losses improves its accuracy, making it reliable and particularly suitable for energy efficiency analysis of the process.

Keywords: Membrane distillation; Water desalination; Mass and heat transfer; Modeling; Spiral wound membrane

1. Introduction

Supplying fresh water for domestic consumption is a global issue. It is reported by the International Desalination Association [1] that globally produced desalinated water is approaching 86.8 × 10^6 m^3/d, benefiting 300 million people worldwide. The water demand is rising mainly because of exponentially growing population and the fast industrialization. In addition, the standard of living is improving [2]. The situation is more critical in arid countries such as Kingdom of Saudi Arabia and other Gulf countries which rely heavily on expensive desalination technologies, such as multi-stage flash (MSF), multiple effect distillation (MED), and reverse osmosis (RO). With increasing energy costs, pursuing alternative low cost and energy-saving water purification processes becomes an imperative. Geothermal underground water is another water source and an economical alternative to costly desalinated water. Studies show that Saudi Arabia has a surplus of warm springs and aquifers where the water temperature can reach to 120°C [3–6]. In due course, the thermal energy of the groundwater can be exploited to operate membrane distillation (MD) processes. MD is a contemporary membrane technology that is suitable for various separation applications [7,8]. Particularly, this membrane process has promising potential for saline water desalination and wastewater treatment [9,10].

MD technology is available in different configurations with the direct contact membrane distillation (DCMD) configuration being the most studied. It has the potential for versatile applications [9,11–13]. The appealing characteristics of DCMD configuration, which are given in several works [14–19], include simplicity, low external energy requirements, the total rejection of solutes, and insensitivity to feed salinity. An attractive feature of water desalina-

*Corresponding author.

tion by DCMD is the production of ultra-pure water. MD is a thermally-driven transport process where only water vapor molecules diffuse through the pores of the hydrophobic membrane. Consequently, all other particles, such as dissolved ions and other nonvolatile species, are retained [20,21]. Another well-known advantage of MD utilization in desalination is the low energy consumption as it operates around atmospheric pressure and at feed temperatures ranging from 35 to 80°C. In fact, such a process can be driven by waste, solar, wind, or geothermal energy [15,22]. For instance, operating the MD for desalination using solar energy has been studied and reported [23–27]. In addition to these attractive features, it is a suitable alternative for conventional desalination technology, especially in remote isolated areas where proper infrastructure and continuous energy supply are not available [28]. Because the MD process is driven using low-grade energy sources, it is particularly suitable where geothermal sources are available. Kalogirou [29] reviewed the use of geothermal energy in saline water desalination.

Another key factor when comparing MD to other existing technologies is the cost. Since MD utilizes low grade energy sources, such as industrial waste heat, solar and geothermal sources, the cost of produced water can be lower compared to conventional thermal desalination processes. It is reported that when waste heat is used, the unit water cost from the MD process can be around 0.64 $/m^3$ compared to 1 $/m^3$ and 1.4 $/m^3$ for large capacity MED and MSF, respectively. It is expected that water cost by MD can be lower than 0.5 $/m^3$ competing with the cost for the RO process [27].

The application of MD for desalination of salty water has been extensively studied. For example, several researchers investigated the MD performance for desalinating brackish and/or seawater experimentally and theoretically [16,17,28,30–33]. These studies involve model development, model validation, mass flux prediction, mass and heat transfer analysis, and performance analysis. Other researchers examined ways to enhance MD performance in water desalination through various arrangements and/or configurations. For example, incorporation of a heat recovery device into the MD system [22,34] and the use of a multistage (or multi-effect) concept [22,35] were proposed. The multistage concept is well known and commonly used in multiple effect distillation and multistage flash technologies. Usually, this strategy is adopted to enhance the recovery ratio and diminish the specific energy consumption of the process. Comprehensive reviews of MD utilization in water desalination can be found in several studies [8,9,36].

Despite the successful review of MD capabilities and advantages, the use of MD technology for large-scale industry is still limited [13,16,17,37]. This can be attributed to several issues, such as membrane properties, the low production rates mainly because of low allowable entry pressure, low recovery ratio due to heat losses via conduction resistance, and fouling and scaling. According to Nakao et al. [17], the commercialization of MD requires additional labscale and pilot plant investigations. As a result, attempts to improve its performance through different means are continuing and are increasingly attracting the attention of researchers.

Almost all reported experimental works on MD operation for water desalination focused on analyzing the variation of the mass flux and/or thermal efficiency as a function of some control parameters such as feed flow rate, feed temperature, and concentration [16–18,28,30–31,38,39]. Mostly, the accuracy of theoretical models to predict water production fluxes is validated in the literature. However, calibrating the model ability to predict the temperature of the exiting streams is not widely studied. The exiting streams for a typical MD unit are the reject brine and hot permeate. Determining the temperature of the exiting streams is useful when performing further detailed energy analyses and energy efficiency evaluations. To the best of our knowledge, experimental results related to the thermal behavior of such processes are neither presented nor discussed although it is an integral part of MD operation. In fact, MD performance in terms of water recovery is governed by coupled mass and heat transfer phenomena. Andrjesdóttir et al. [30] indicated that despite the extensive experimental investigation, a better understanding of the heat and mass transport phenomena needs to be established. The investigation is not complete without understanding the interaction between the material and thermal behavior of the MD operation. Such analysis leads to better design and optimization of such crucial separation processes. In addition, the simultaneous fitting of heat and mass data to a physical model, which is rarely addressed in the literature, can enrich the understanding of the fundamentals of the process and shed light on the deficiencies of exiting mathematical models.

However, modeling the various thermo-physical phenomena inherent to the MD process is not easy since it encounters several challenges. This would explain the various discrepancies and lack of accuracy between the theoretical results and the experimental ones observed in various previous studies. The main challenges can be summarized as follows:

- It is difficult to estimate the real values of some membrane properties, which are in general considered as inputs to the numerical models. For instance, the porosity and tortuosity of the membrane change when the latter is loaded. Camacho et al. [36] reported that under the hydrodynamic pressure associated with the flowing feed and permeate, the membrane can be compressed and its properties, such as porosity, thickness, and pore size, can be altered. Zhang et al. [40] observed a flux reduction of 15%–39% when the pressure in the DCMD is increased from 1 kPa to 45 kPa. In addition, it was reported in several studies that the uncertainty of membrane properties leads to inaccurate mass transfer fluxes.
- The choice of appropriate correlations for the heat transfer mechanism is not straightforward. In fact, the majority of the available heat transfer correlations are developed for different conditions and applications, but not for permeable microporous membranes.
- The mass transfer mechanism within the membrane is complex and not well understood. Several models have been proposed and implemented. It most likely combines simultaneously three modes: Knudsen, molecular, and Poiseuille.

Therefore, the objective of this work is to perform integrated theoretical and experimental analysis of the material and thermal performance of an experimental MD rig. A full-scale spiral-wound MD module is used for the experimental tests. Experimental results showing the effect of feed parameters, temperature, flow rate, and salinity, are presented and discussed. Furthermore, a theoretical model is calibrated using the experimental data and an experimentally validated model for accurate prediction of MD performance is obtained. Such a reliable model is suitable for energy efficiency analysis, which is an essential part of sustainable operation and development.

2. MD pilot plant description

Fig. 1 is a pictorial of the MD pilot plant manufactured by SolarSpring, Germany. The module is equipped with a direct contact MD (DCMD) module, which is characterized by a 10 m² effective membrane-area, 230 µm thickness of membrane, 14 m channel-length, and 0.7 m channel-height, 0.2 µm pore diameter, and 2 mm channel-gap. The pure water production of the unit depends on several variables including the operating conditions of the feed solution, such as volume rate, salinity, and temperature. The module is equipped with a programmable logic controller (PLC) responsible for control and data acquisition. A computer connected to a web server with human-machine-interface (HMI) is available for experimental data collection, storage, and analysis. The DCMD has four hydraulic circuits. The flow sheet for the process is illustrated in Fig. 2.

Fig. 1. SolarSpring MD module.

The evaporator circuit is filled with the feed medium, which is usually brackish water [evaporator tank T1]. The evaporator circuit can be operated at 30–80°C and 0–700 L/h as the feed temperature and volume flow, respectively. The raw brackish water can be heated to the desired temperature in the heat exchanger H1. The necessary heat is supplied to H1 via an electrical heater in the heating circuit, which is controlled by a PLC. The condenser circuit has to be filled with tap water [condenser tank T2] of natural pH and conductivity in the range of 5–500 µS/cm. The volume flow is the same as in the evaporator circuit and is controlled by a PLC. The temperature of the cold stream is maintained in the heat exchanger H2. The cooling demands for H2 are supplied externally by a coldwater stream in the cooling circuit. The temperature of the cooling circuit is controlled manually using the valve A.015. The automatic control of the condenser circuit's temperature is foreseen with the temperature sensor TCI.009 (measurement at the DCMD module's condenser inlet). The vaporized water condenses in the condensation circuit where it leaves with the cold stream. Therefore, it is separated through an overflow, and collected and measured in the product tank T3. The electrical energy demand of the unit is supplied externally over a power point plug (50/60 Hz, Numbers of poles: 5, Current: 32 A, Voltage: 400 V, Protection class: IP 44, male connector). The unit is protected against overpressure and low levels in the main tanks.

3. MD Description, model, and simulation

The separation in the DCMD unit that produces pure water occurs at microscopic scale as shown in Fig. 3. A typical MD contains a hydrophobic membrane in the middle where cold and hot streams of water flow on counter-currently either sides. The thin membrane layer allows the passage of vapor molecules through its pores and retains liquid water. The hot stream is usually saline water with a bulk temperature T_h. On the other side, a cooler stream flows with a bulk temperature T_c. Because of convection and conduction resistances, the corresponding temperature of the hot and cold sides at the membrane surface is much lower and denoted as T_{mh} and T_{mc}, respectively. The difference between T_{mh} and T_{mc} creates a vapor pressure difference, which causes vaporization of the water on the hot side. The vapor migrates through the membrane pores and condenses on the cold permeate side. Accordingly, ultrapure water is produced. A major challenge that limits the MD unit performance is that the temperatures difference on either side of the membrane ($T_{mh} - T_{mc}$) is lower than its corresponding bulk value ($T_h - T_c$) because of the resistance to heat transfer by convection and conduction. This phenomenon is known as temperature polarization, which is analogous to concentration polarization. The temperature polarization reduces the driving force for mass transfer, downgrading the efficiency of pure water recovery.

Clearly, water separation in the MD process is overseen by simultaneous heat and mass transport mechanisms. Several researchers developed steady-state models to mathematically describe the heat and mass transport operations in MD units [16,17,28,30–33]. These models are conceptually the same, where mass and heat fluxes are defined using first principles and correlations from which the pure water

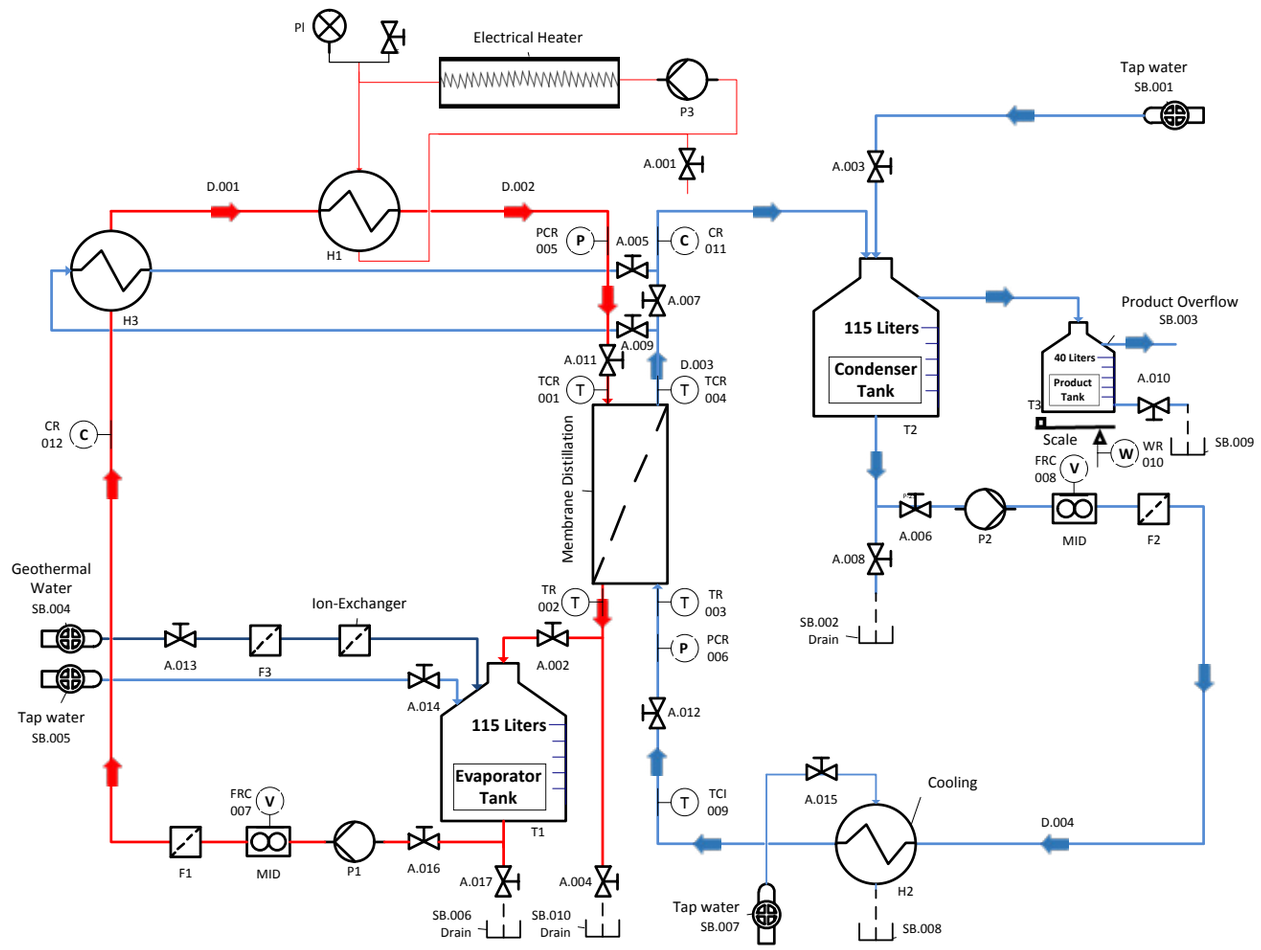

Fig. 2. Schematic of the experimental setup of the MD process flow sheet.

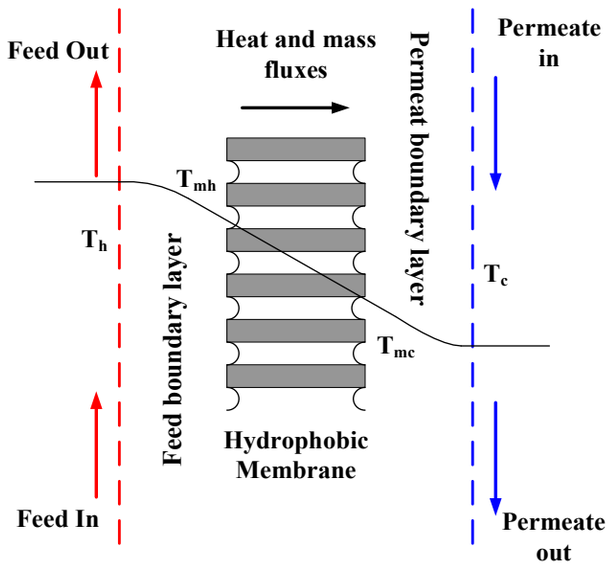

Fig. 3. Boundary layer for a typical DCMD.

production is estimated. Since developing a new model is not the intention here, the model proposed by Nakoa et al. [17] will be used. This model has been widely used in previous studies [28,30–33,41]. The detailed derivation of the MD model is listed in the Appendix.

The algorithm for solving the MD model equations is shown in Fig. 4. In this case, the feed flow rates and the feed temperatures are specified. However, the exit temperatures, $T_{h_{out}}$ and $T_{c_{out}}$ as well as the membrane surface temperatures, T_{mh} and T_{mc}, are unknown. Although $T_{h_{out}}$ and $T_{c_{out}}$ are measured in our device, it is expected that the model should be able to predict them from the other given operating conditions. Therefore, the solution protocol is iterative in nature involving two iteration loops. The outer iteration loop fixes $T_{c_{out}}$ while the inner iteration loop fixes the membrane surface temperatures. In due course, the calculation procedure starts by assuming an initial value for $T_{c_{out}}$. Next, for the given value of $T_{c_{out}}$, the membrane surface temperatures are also assumed, and the heat transfer equations are solved until they reach convergence, e.g., the condition (A.10) is satisfied,which implicitly specifies the membrane surface temperatures. Next, the heat balance equation of the hot side is solved to obtain $T_{h_{out}}$. Similarly, the heat balance equation

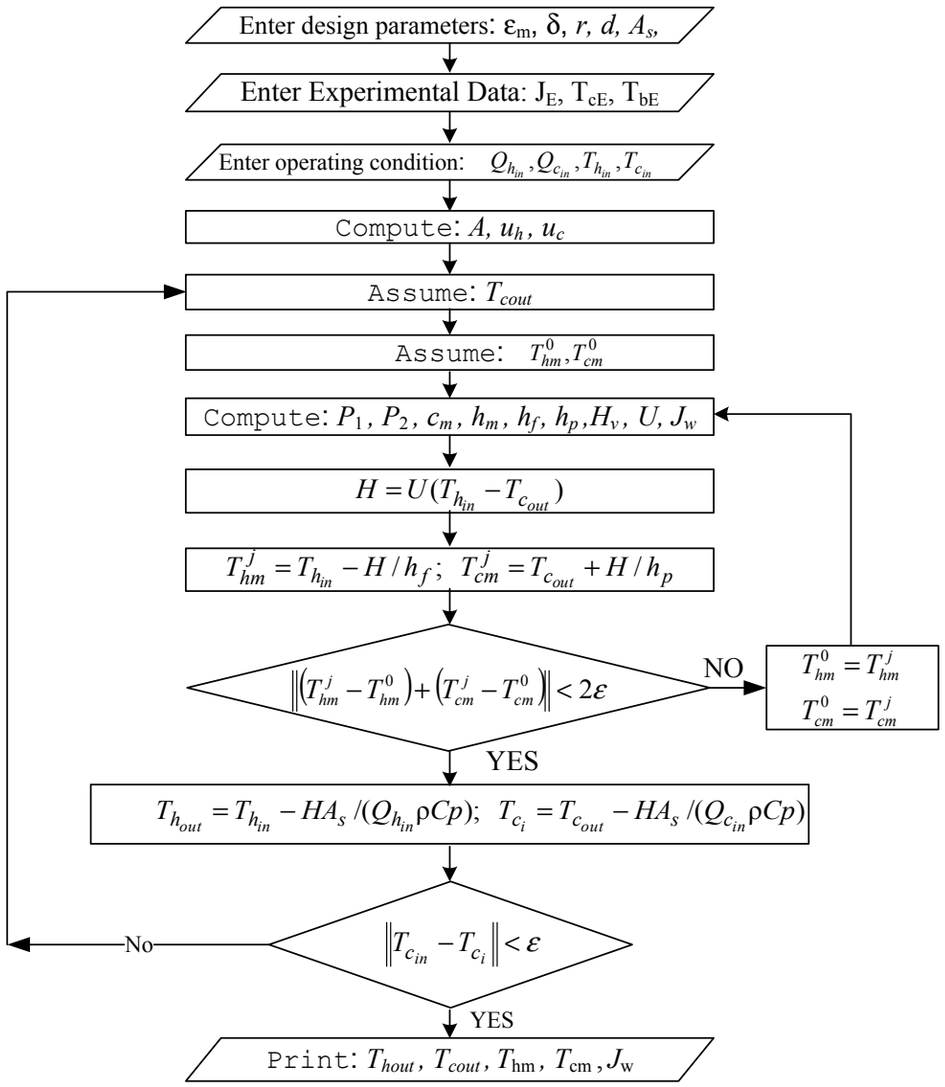

Fig. 4. Organigram for model solution.

of the cold side is solved to obtain T_{c_i} (inlet permeate temperature). Since T_{c_i} is prespecified, the calculated T_{c_i} should match the predefined value. If they match, the solution is found, otherwise another value is assumed for $T_{c_{out}}$ and the entire procedure is repeated till convergence occurs. This algorithm is used by Zhang [41] and others. To generate a predictive model over a wide range of operating conditions, the solution algorithm is modified to account for the model-plant mismatch as shown in Fig. 5. In this case, the model parameters should be modified such that the model predictions adapt to the variation in feed flow rate and brackish water temperature. In particular, we choose to adapt the membrane porosity and heat losses from the water flowing on either side of the membrane. Note that the factors a_2 and a_3 in the organigram are related to the heat losses as follows:

$$a_i = \frac{1}{1-f_i}; \quad i = 2,3 \tag{1}$$

where f is the ratio of the heat loss to the heat released from the hot stream as follows:

$$f = \frac{heat\ loss}{m_h Cp_h\left(T_{h_{in}} - T_{h_{out}}\right)} \tag{2}$$

A further discussion of the adjustment of the model parameters to fit the experimental data will be given in the discussion section. It should be noted that the solution procedure remains conceptually the same as in Fig. 4 with the inner loop unchanged. An exception is the outer loop, which involves additional unknown parameters that are the tuning factors, a_1,a_2, and a_3. In addition, the termination criteria of the outer loop need to include minimization of the model-plant discrepancy in terms of mass flux and exit temperature of both operating streams. Minimization of the difference between the model and plant exit permeate temperature is found to be essential at low flow rates. At high

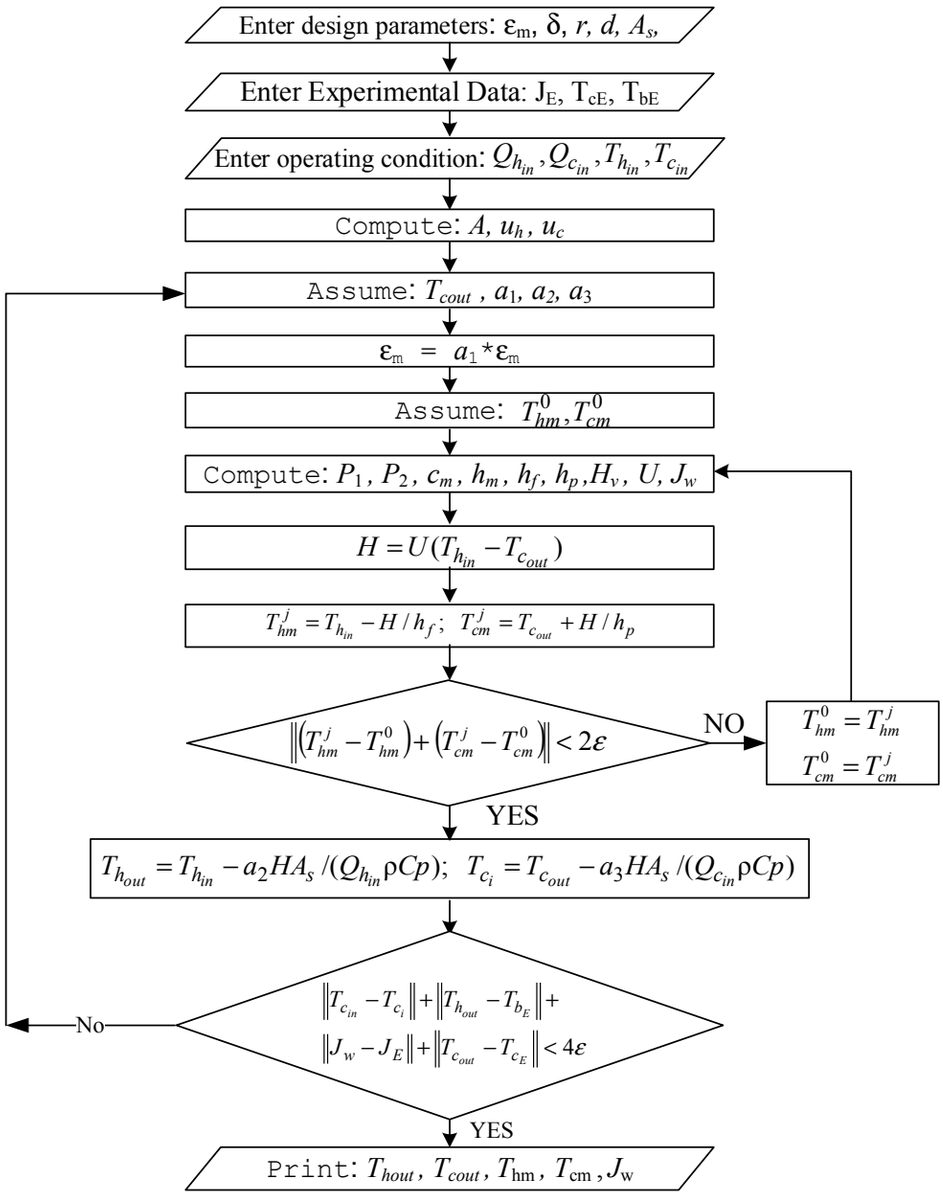

Fig. 5. Organigram for model solution and fitting of experimental data.

flow rates, this term is unnecessary; in fact, strictly enforcing it leads to an infeasible solution. Note that all calculations are carried out using MATLAB® version R2010a. The convergence tolerance is taken as $\varepsilon = 1 \times 10^{-7}$.

4. MD plant operation

Fig. 6 illustrates the real time operation of the MD process. The rig is operated at a feed flow rate of 150 L/h and a temperature of 80°C for the hot feed stream. The inlet condenser temperature is controlled at 25°C in the cooling circuit using tap water. The process needs 15~45 min to reach steady state depending on the feed temperature. The exit temperature of the cooling stream approaches 70°C at steady state. Because the membrane surface area is sufficiently large, the exit brine temperature at equilibrium is very close to the condenser inlet temperature. In fact, for this particular MD unit, as an equal feed flow rate is employed for both sides and the inlet temperature of the cold stream is fixed at 25°C, the hot stream is always cooled to around + 1~4°C depending on the magnitude of the feed flow rates and the inlet temperature of the hot stream. The right side of Fig. 6 depicts the mass of the collected distillate. The production rate is simply estimated by dividing the accumulated distillate weight by the time elapsed during steady state. It should be noted that although the process allows for high flow ratesup to 700 L/h, our experiments will be

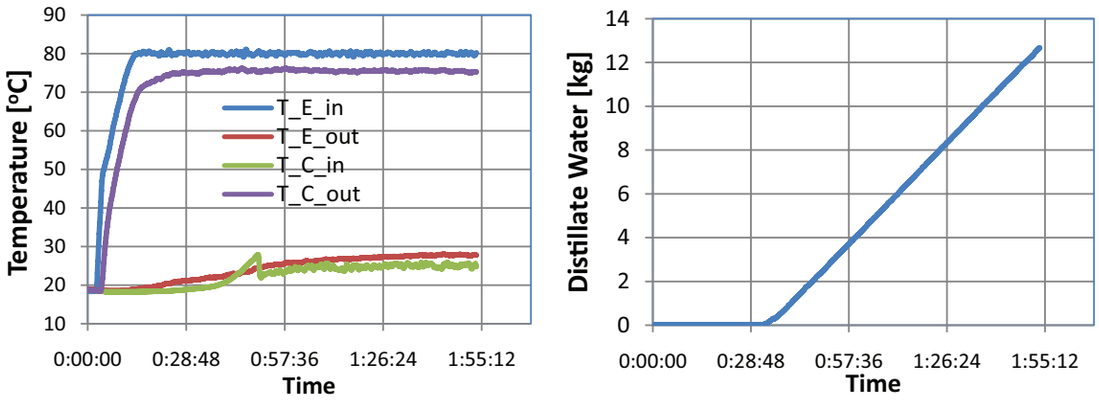

Fig. 6. Typical experimental profile for $Q_{h_{in}} = Q_{c_{in}}$ = 150 L/h, $T_{c_{in}}$ = 25°C, $T_{h_{in}}$ = 80°C, and 0.05% salinity.

confined to 300 L/h. This is because at a higher flow rate, the manually-controlled cooler system cannot maintain the inlet temperature at 25°C. The SolarSpring MD unit has been tested by others [28,42,43].

5. Experimental results analysis

5.1. Thermal analysis

Different experiments are carried out at selected values for the feed flow rate, feed temperature, and salinity. The temperature of the cold stream feed is controlled at 25°C and the salinity of the raw water feed is fixed at 0.05 %. The idea is to examine the effect of the feed flow rate, temperature, and salinity on the material and thermal behavior of the process. Almost all reported literature focusses on the mass flux behavior of MD modules; while the heat flux is an integral part of the separation process. Fig. 7 shows the steady-state variation of the experimental data for exit permeate temperature with hot feed temperature at different flow rates. The figure includes the temperature difference at both ends of the MD module, i.e., at the entrance and exit. The diagram includes error bars representing the measurement uncertainty, which is more apparent in the temperature difference curves because of the plotting scale. The error bars represent the standard of deviation of several repeated experiments to average and lump the random errors and systematic errors. As shown in Fig. 7a, $T_{c_{out}}$ increases linearly with hot feed temperature for all flow rates. However, as the flow rate is increased beyond 100 L/h, the heat transfer saturates; i.e., $T_{c_{out}}$ cannot exceed a maximum value because the resistance induced by convection and conduction reaches a minimum value neglecting the energy loss due to radiation. The $T_{c_{out}}$ profile versus flow rate is also shown in Fig. 7d to clarify how it saturates at flow rates higher than 150 L/h for all operating feed temperatures. The *bulk* temperature difference ($\Delta T_b = T_{h_{in}} - T_{c_{out}}$) at the MD entrance side escalates too as shown by the deviation plot in Fig. 7b. However, the temperature difference increases linearly at high flow rates and monotonically at lower flow rates. At high flow rates, ΔT_b becomes small in magnitude and constant with flow rate. This indicates that heat resistance reached a fixed value and that the system has a very good heat transfer capability. In fact, both Fig. 7a and 7b show a transition region that occurs between 100 and 150 L/h. When operating the MD at inflows higher than 100 L/h, the heat flux is enhanced by an amplified Reynolds number due to large circulation rates leading to a further warm up of the permeate stream. This situation is manifested in higher values for $T_{c_{out}}$ and consequently smaller temperature differences, ΔT_b. The transition behavior is obvious in the response of the temperature difference at the exit ($\Delta T = T_{h_{out}} - T_{c_{in}}$) as depicted in Fig. 7c. However, it is in the opposite direction, i.e.,a smaller temperature difference at a lower flow rate. In addition, the temperature difference ΔT is minor in general and becomes even trivial at lower flow rates. This means the water in the evaporator circuit loses almost all its sensible heat because of its sufficiently large surface area as mentioned earlier. At low flow rates, the heat loss is even greater because of the increased residence time, but it is not necessarily due to the warming of the water flowing out. This is because the $T_{c_{out}}$ profile at the lower flow in Fig. 7a is less than that at the higher flow rates. In fact, a greater heat loss to the surroundings is anticipated because of a longer residence time induced by the low circulation rate. At higher circulation rates, the brine exits the system slightly warmer. It can be argued that the reduction in residence time affects the energy consumption. Furthermore, the temperature drop at the hotter end (bulk channel) is larger than that at cooler end. This can be attributed to the fact that heat gained by the permeate stream is limited by the heat loss due to conduction and radiation to the atmosphere. Nevertheless, regardless of the flow rate, the heat losses prevail allowing the brine stream to cool significantly. In some cases, temperature fluctuations exist because the inlet temperature of the cold stream is manually controlled. Manual control of $T_{c_{in}}$ may become a bit challenging at elevated temperatures and/or flow rates. The temperature profiles shown in Fig. 7 indicate steep changes. However, these variations cannot be attributed to the existence of a transition region from laminar to turbulent flow because our entire operation lies within the laminar region. In Fig. 7b, the steep increment at a low flow rate can be attributed to the greater residence time. The average percent increment in ΔT_b at low flow rates is 180 % compared to 150 % at high flow rates. Furthermore, the sharp changes in Fig. 7c can be explained by the uncertainty associated with T_{c_i} due to manual regulation. Manual

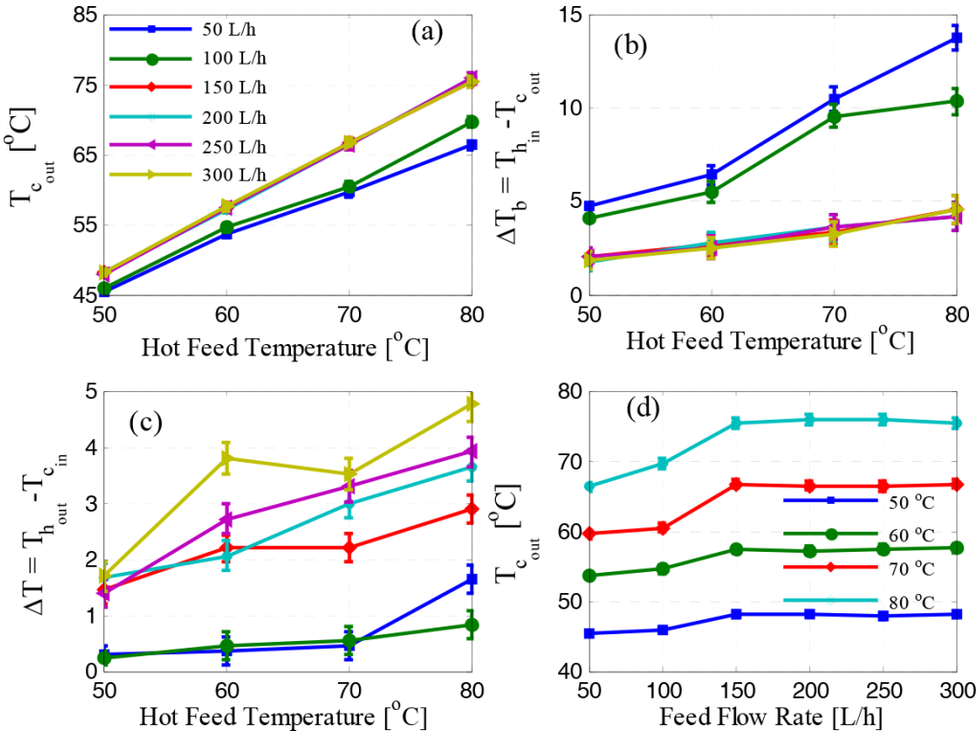

Fig. 7. Exit permeate temperature at steady state at various feed flow rates and temperatures, $T_{c_{in}}$ = 25°C and 0.05% salinity.

adjustment of the inlet cold temperature becomes more difficult at higher flow rates and feed temperatures. The percent increment in ΔT at low flow rates is approximately 360 % compared to 144 % at higher flow rates.

5.2. Mass production analysis

Fig. 8a illustrates the experimental data representing the effect of feed flow and hot feed temperature on the mass flux of the purified water. The salinity of the processed water remains at 0.05%. The positive influence of increasing the water circulation and/or inlet temperature is intuitive. For a given feed flow, as the hot feed temperature rises, the driving forces for vaporization governed by the temperature difference at the membrane surface ($\Delta T_m = T_{mh} - T_{mc}$) grow accordingly, leading to enhanced mass flux through the membrane. The increment of the driving force is directly proportional to the vapor pressure that increases exponentially with temperature [16,18,30–32,38]. Specifically, as shown in Fig. 8a, with an increase in the inlet temperature from 50°C to 80°C, the measured permeate flux rises by 1.07 kg/(m²·h) (equivalent to 167%) at 300 L/h and 0.17 kg/(m²·h) (equivalent to 154%) at 50 L/h. The permeate flux is promoted at higher flow rates mainly due to hydrodynamic enhancement by the circulation rate but not due to the temperature driving force as Fig. 7b indicates small and fixed ΔT_b at high flow rates. This behavior will be discussed further in the model validation section by examining the transmembrane temperature and polarization obtained by numerical solution of the mathematical model.

In contrast, escalating the flow rate improves the mass flux due to the enhancement of mass and heat transfer coefficients but largely due to amplified throughput. The latter is evident as depicted in Fig. 8b. The recovery ratio, which is the ratio of the water production to the feed flow rate of the brackish water, is almost invariant with increasing inflow. Minor drifts occur at low flow rates that are related to the transition behavior mentioned earlier, but they settle afterward. Infact, one can consider that the recovery ratio reaches a maximum value at 150 L/h. At lower flow rates, the mass flux and, consequently, the recovery ratio are low, which contradicts the trend of the temperature difference shown in Fig. 7b. Assuming the bulk temperatures of the cold and hot side are proportional to the end temperature, i.e., $T_{c_{out}}$ and $T_{h_{in}}$, respectively, the temperature difference at the membrane surface deceases as flow rate increases. This situation decreases the driving force and the mass flux, which does not support the results of Figs. 8a,b. Therefore, we conclude that the end temperatures do not represent the bulk temperature profile along the membrane length faithfully. We suggest that, at high flow rates, the bulk temperature profile becomes uniform due to improved hydrodynamics leading to enhanced mass flux.

The effect of increasing the feed (i.e., hot) flow rate on the mass flux is positive as observed and well explained by many researchers [16,18,28,30–32,38]. They all agree that raising the feed flow will improve the turbulence manifested by the Reynolds number that in turn will increase the feed heat transfer coefficient leading to a further rise in the membrane surface temperature and reducing the temperature polarization effect. This causes larger driving forces

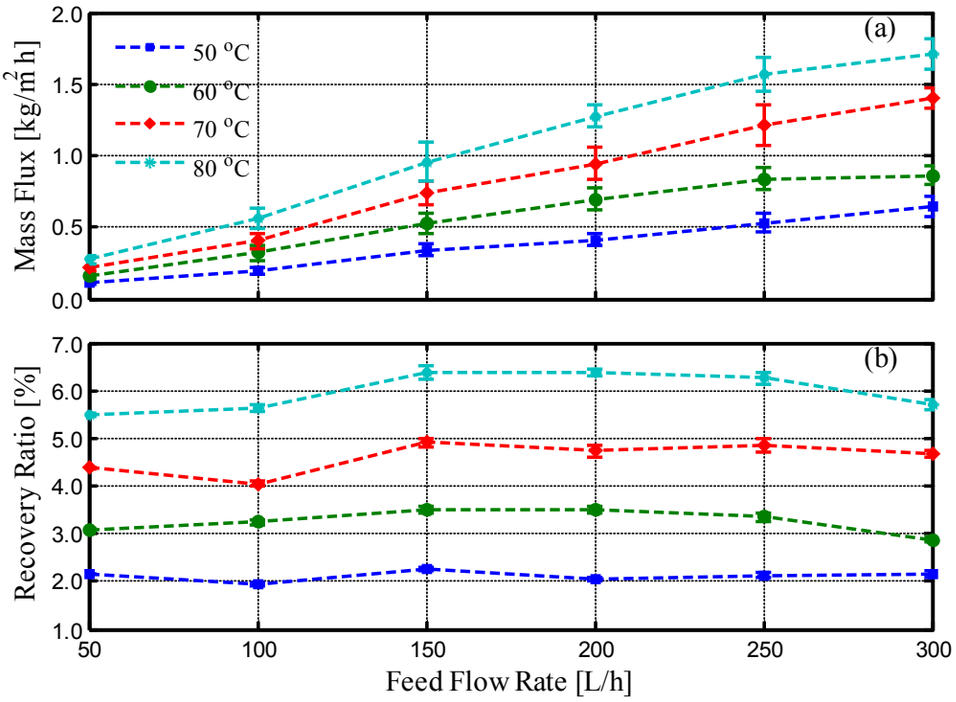

Fig. 8. Measured mass flux and recovery ratio at various feed flow rates and feed temperatures, $T_{c_{in}}$ = 25°C and 0.05% salinity.

and permeate fluxes. In addition to the above interpretation, Alanezi et al. [31] suggests that the turbulence growth reduces the heat transfer resistance at the membrane interface and consequentially increases the mass transfer coefficient. Similarly, Winter et al. [28] believes the effect of feed flow on mass flux is controlled by two phenomena. The first is the influence of the enhanced hydrodynamics as mentioned by the other researchers. Secondly, the increased feed flow will result in amplification of the total thermal energy entering the feed channel causing a larger *bulk* temperature difference across the membrane.

Nevertheless, in our case, the flow rate increases on both sides simultaneously. Therefore, the phenomena described earlier should occur on both sides leading to an asymptotic trend as the flow rate exceeds 100 L/h. As mentioned previously, when the circulation rate grows, the exit permeate temperature reaches its maximum achievable value allowing the temperature difference ΔT_b to reach steady state. This situation limits the MD performance. A similar observation is also reported by Fard et al. [32] and Boughuecha et al. [38] as they find that mass flux reaches an asymptotic value beyond which the flux cannot be increased further as the circulation flow increases. Boughuecha et al. [38] attributes this behavior to the gradual increase in the convective heat transfer for both sides at the membrane boundary layer. As a result, the temperature polarization coefficient diminishes leading to the mass flux limitation.

5.3. Effect of salinity

The tests described in the previous section were conducted using tap water with very low salinity. To study the effect of salinity on DCMD performance, we conduct the experiments using synthesized salty water at 10000 ppm. The trend of permeate temperature and mass flux is shown in Fig. 9. Fig. 9a demonstrates only the temperature response for the high salinity case for clarity. Because the difference between the T_c trends at high and low salinities is marginal, plotting them in one graph creates overlapping curves. This, in fact, confirms the insignificant influence of salinity on the heat transfer efficiency; e.g., salt does not hinder energy transfer from the hot side to the cold side. Nevertheless, the transition behavior is still observed even in the presence of dissolved compounds in the feed solution. In contrast, Fig. 9b illustrates how water production is clearly affected by impurities. Mass flux deterioration cannot be attributed to temperature drop across the membrane because it is invariant as mentioned earlier. Salt particles may adversely alter the latent of heat vaporization and/or the membrane permeability causing downgraded mass flux. According to Tzahi et al. [39], the presence of high concentration salt in the feed solution creates an additional boundary layer at the membrane surface. This phenomenon will further degrade the driving force for vaporization. However, they conclude that the presence of salt in the feed has a marginal effect of the MD performance as they report an average of 9% flux decline when the salt concentration is increased from 0.06% to 7.3%. In our case, an average of 12% flux degradation is observed. Fard et al. [32] also attribute water production deterioration in the presence of salt to the development of a boundary layer that affects the mass and heat transfer coefficients and, consequently, the concentration polarization. This situation results in reduced water vaporization and flux. Additionally, it is observed in

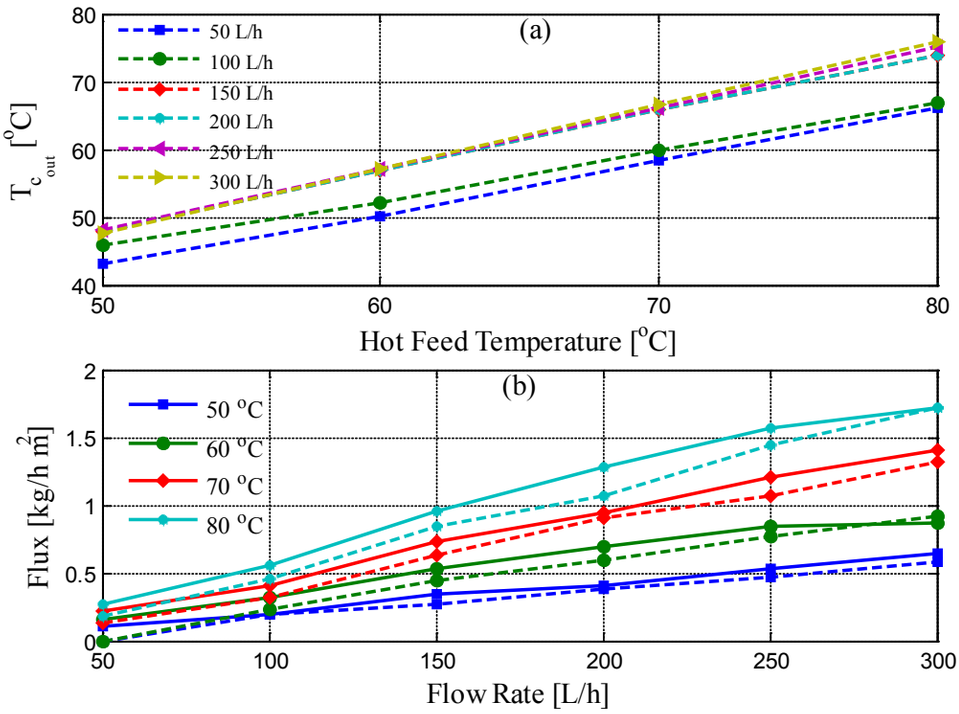

Fig. 9. Experimental mass flux and exit permeate temperature at different operating conditions, $T_{c_{in}}$ = 25°C; solid: salinity = 0.05%, dashed: salinity = 1%.

Fig. 9b that the impact of salinity diminishes at a high flow rate for all feed temperatures. It is believed that the elevated flow rate enhances the turbulent conditions and decreases the boundary layers resulting in improved performance. Interestingly, as illustrated in Fig. 9b, the membrane unit has negligible freshwater production at very low operating conditions of feed temperature of 50°C and flow rate of 50 and 100 L/h.

5.4. MD model validation

Next, we calibrate the adopted MD model to the experimental data. A black box (empirical) model can be easily fitted to the data. However, fitting a first principle model is of interest because it helps to understand the underlying physics of the process. Moreover, the calibration process highlights any shortcomings associated with the physical model. Figs. 10 and 11 demonstrate the simultaneous calibration of the model thermal and material predictions. The mass prediction is represented by the mass flux of the fresh water. The heat prediction is manifested by the exit permeate temperature and the exit brine temperature. The latter is not shown for simplicity. The model is fitted using experimental data for all flow rates and feed temperature shown in Fig. 7. To achieve an acceptable model-plant match, three process parameters are adjusted: the porosity (ε) and heat losses on the hot and cold sides (f_1, f_2). To obtain a predictive model, global values for the tuning parameters that cover the flow rate range of 150~300 L/h and temperature range of 50~80°C are determined as ε = 0.65, f_1 = 28.5%, and f_2 = 25.6%. For the feed flow range of 50~100 L/h and temperature range of 50~80°C another a unique set of values is obtained as ε = 0.47, f_1 = 18.3%, and f_2= 20.2%. Note that two sets of tuning parameter values depending on the flow rate range are used because of the transition behavior mentioned earlier. Figs. 10 and 11 show perfect model-plant matches in terms of mass flux and exit permeate temperature except for very low flow rates of 50 L/h, which indicates the model limitation at very low flow rates. It should be emphasized that this prediction accuracy cannot be achieved using the raw model. Adjustment of the model parameters was necessary. Regarding $T_{c_{out}}$ and $T_{h_{out}}$, Eqs. (A.11) and (A.12) were not able to correctly capture the actual behavior of the process. These equations assume that the entire energy lost from the hot stream is transformed into total heat flux that absorbed by the membrane material and provided as heat of vaporization. Similarly, it is assumed that the exact amount of energy is consumed to warm up the permeate stream. In reality, heat losses on both sides occur. Much heat loss occurs due to the conduction through the membrane [9,18,38,39]. Boughuecha et al. [38] examine the heat loss to the surroundings and estimate a range from 0.58 kW to 0.93 kW when the MD is operating around 60°C. Therefore, the proposed MD model is modified to account for the heat loss to the surroundings. The heat loss is assumed to be a fraction of the total heat extracted from the hot stream.

For analysis purposes, we examine the model calibration at each operating point. The idea is to study the effect of the process tuning parameters on process behavior. Fig. 12 illustrates how the assumed heat deficits are adjusted to

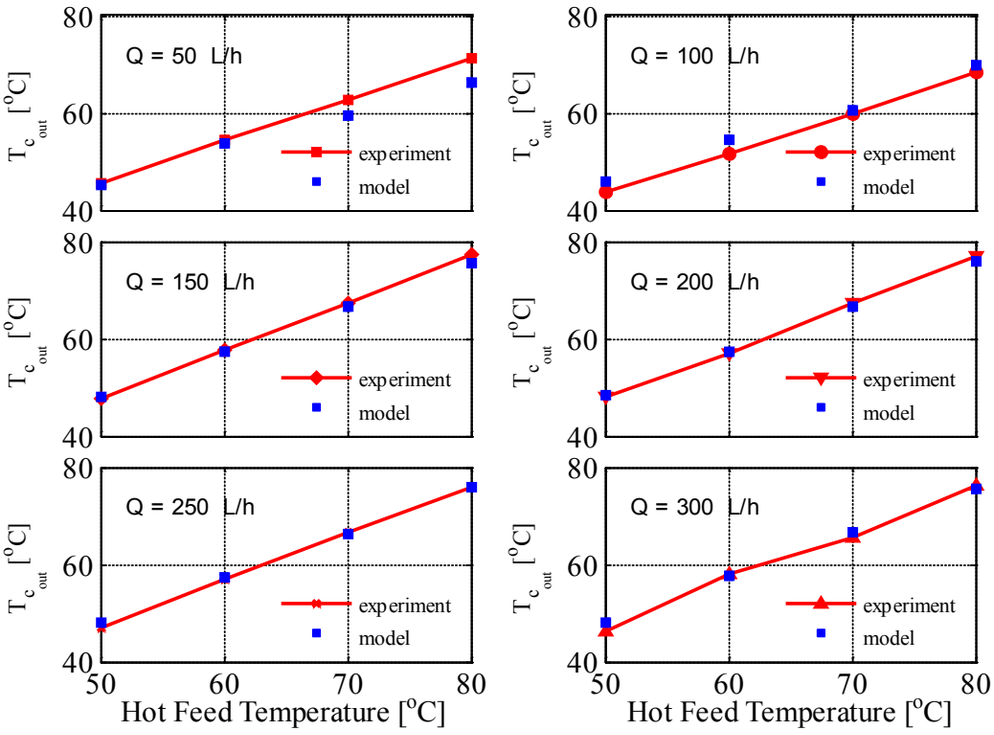

Fig. 10. Model validation of exit permeate temperature at different operating conditions, $T_{c_{in}}$ = 25°C, salinity = 0.05%, ■: 50 L/h, •:100 L/h, ◆: 150 L/h, ▼: 200 L/h, ×: 250 L/h, ▲: 300 L/h.

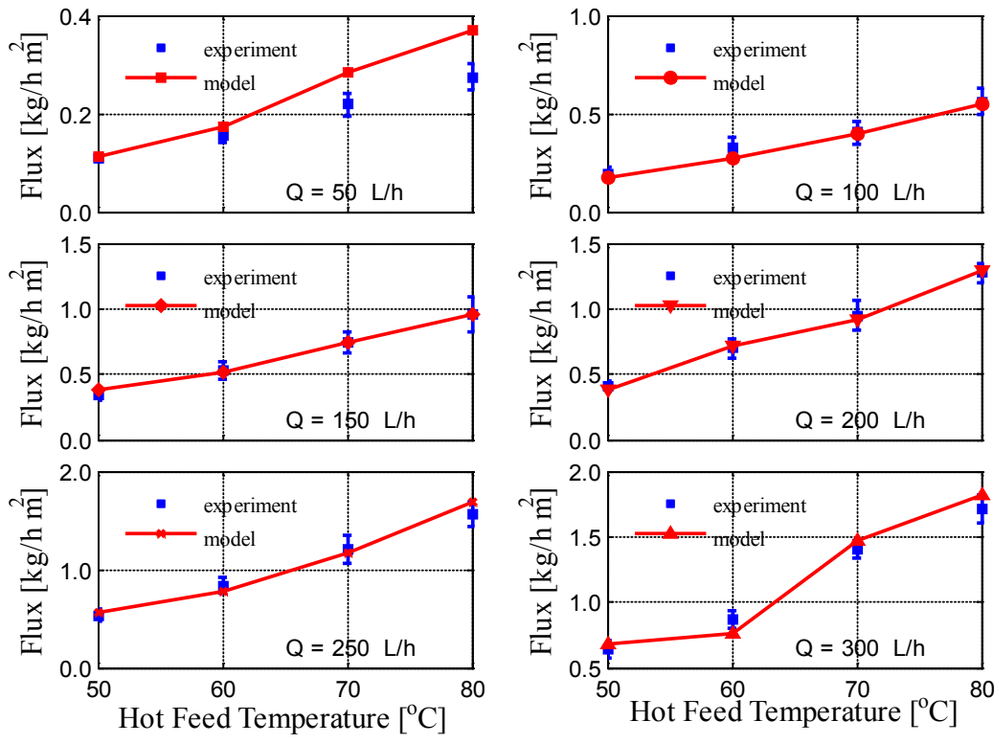

Fig. 11. Model validation for mass flux at different operating conditions, $T_{c_{in}}$ = 25°C, salinity = 0.05 %, ■: 50 L/h, •:100 L/h, ◆: 150 L/h, ▼: 200 L/h, ×: 250 L/h, ▲: 300 L/h.

make the model prediction for $T_{c_{out}}$ and $T_{h_{out}}$ match their corresponding experimental values. We observe that heat loss at the permeate side is relatively larger than that at the hot side; and at high flow rates, the deficit increases as hot feed temperature increases, which is rational. Interestingly, the heat losses at lower flow rates decrease with the inlet temperature of the treated water to match the experimental value of $T_{c_{out}}$ at a low flow rate, which is lower than that at a high flow rate. This behavior is incomprehensible; however, it is an attempt to cure a model deficiency. Indeed, the model cannot adequately capture the effect of lowered circulation rate on the heat transfer coefficient. The reason for this failure is the mass and heat interaction, as a variation in the heat transfer coefficient will also affect the mass flux through Eq. (A.1). Andrjesdóttir et al. [30] study the mass and heat transfer in flat sheet MD and conclude the necessity for better heat transfer correlation to more accurately predict the fluxes in DCMD.

Regarding the mass flux, Eq. (A.1) is also modified to improve the model accuracy particularly for tracking the measured mass flux. Mathematically, *J* is estimated from the product of the permeability coefficient by the pressure difference across the membrane boundary layer. Both terms counteract creating difficulty in adjusting *J* to match the real data. The pressure difference is indirectly influenced by the heat transfer coefficient, which is affected by both flow rate and temperature. The permeability coefficient is affected by the interface temperature and also by the membrane properties, such as thickness, tortuosity, and porosity. Therefore, it was necessary to adjust the permeability coefficient via the porosity to reflect the impact of flow variation on the mass flux. Porosity is chosen for calibrating the model prediction of the mass flux because it is believed to have a significant effect on the permeate flux [9,18,39,22]. In addition, Rao et al. [44] indicates that because of hydrostatic pressure, membrane compaction may occur. This behavior will affect the membrane structural properties, such as δ, τ, and ε_m, which will in turn influence the mass transfer operation. Fig. 12 depicts the calculated necessary variation of porosity to improve the model precision over the entire range of operating conditions. The calculated porosity at high flow rate was found to increase with inlet hot temperature, indicating that membrane porosity may expand with heat. Similarly, porosity is supposed to increase with the flow rate due to turbulent conditions that reduce the boundary layer. In contrast, at low flow rate, the porosity is lower, and, furthermore, it decreases with $T_{h_{in}}$. It should be noted that the enlargement of porosity remains hypothetical. It increases because it is chosen to adapt the model for the model-plant mismatch, otherwise another process parameters could be the reason for flux enhancement at higher bulk temperature. The calibrated porosity shown in Fig. 12 ranges from 0.4 to 0.8, which is reasonable as microporous membranes with porosities of 80 % and higher are available commercially [39]. Deformation of the porosity at high and low flow rates could be possible, but the large variation indicates the limitation of the model to capture the process behavior over a wide range of operating conditions. The calibration of the MD model to address the combined effect of mass and heat transfer is studied by others [10,21,30]. Alklaibi and Lior [10] uses a two-dimensional conjugate model to describe the mass and heat transfer to improve the model's flux prediction. Ho et al. [21] introduces corrective factors in their model for both heat and mass transfer to better correlate the model for a roughened surface membrane. Andrjesdóttir et al. [30] allows their model to select the best correlation for heat transfer to enable the model prediction to match the experimental data. Chen et al. [45] indicates that most investigators have adopted macroscopic models to predict DCMD performance. Such models cannot predict accurately the temperature polarization, which requires the evaluation of the interfacial temperatures. They propose a two-dimensional model to predict with better accuracy the temperature polarization profile. Recognizing the complexity of the mass transfer phenomenon within the membrane, the investigators introduce correction coefficients in the water vapor flux expression. These coefficients, called the Knudsen diffusion model and Poiseuille flow model contributions, were selected to establish fair agreements between the theoretical and experimental values. Recently, Karanikola et al. [46] studies the effects of membrane structure and operational variables on MD performance. Experimental tests and numerical simulations are performed on a sweeping gas flat sheet MD unit. The model is calibrated using experimental data while the tortuosity is taken as the sole fitting parameter. Tortuosity values are selected to minimize the difference between the predicted and measured water production rates. Model validation is then performed by considering the variation of the permeate production with the sweeping gas velocity and temperature. Similarly, Nakoa et al. [17] introduces in their model an evaporation correction factor relating the evaporation rate and the salinity. The results show that the new corrected mass flux values using the evaporation correction factor have less deviation from the measured data than the first theoretical values obtained with the original model.

According to Fig. 12, the model parameters should vary with each operating condition to obtain perfect model predictions over a wide range of control parameters. However, a model with variable design parameters at each point is impractical. Alternatively, only two sets of values can be used for the entire domain as discussed earlier with a slight loss of accuracy at low flow rates as shown in Fig. 10. Otherwise, these parameters can be correlated to the entire range of operating conditions to formulate a unique adaptive function. Incorporating this function into the MD model equations makes the model predictive as well as adaptive to variation in both feed flow rate and temperature. Another way to improve the model predictions is to consider a different model structure. For example, the bulk temperature in the cold and hot sides should vary with the membrane length especially for this MD unit with a large surface area where the temperature drop from the inlet to the outlet can reach 50°C. In fact, Eleiwi et al. [47] shows that the bulk temperature is not homogeneous throughout the membrane thickness and length.

Having developed the mathematical model, internal variables that cannot be measured such as the trans-membrane temperature and membrane permeability can be estimated using the model. Fig. 13 illustrates the response of some of the unmeasured process characteristics. The first notable observation is that the transition regime is apparent for all process parameters. Secondly, the temperature drop at the membrane interface ΔT_m is higher at lower circulation

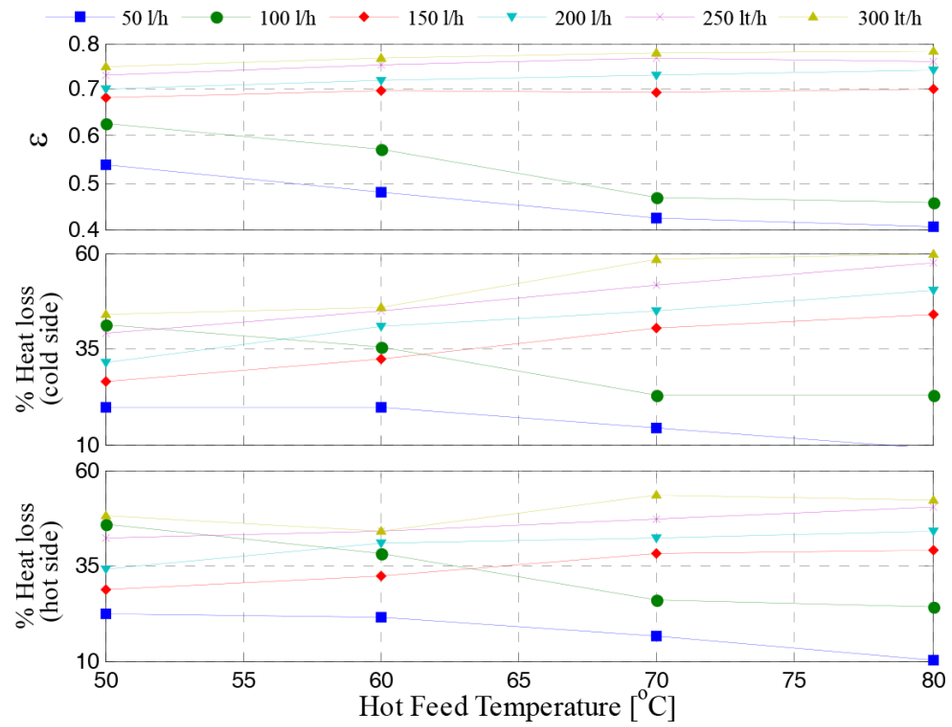

Fig. 12. Calibrated model parameters.

rates as shown in Fig.13a. In fact, at higher flow rates, ΔT_m is almost constant. This behavior is correspondingly reflected in the temperature polarization coefficient (TPC) shown in Fig. 13b. At high flow rates, TPC drops sharply with inlet temperature for the hot stream causing a negative effect on the MD performance. This also means the heat transfer resistance of the boundary layer controls the MD process [13]. The highest calculated TPC is around 0.8, which is less than that reported by Al-Anezi et al. [31](0.87~0.93 at 60°C feed temperature). Unlike our findings, Al-Anezi et al. [31] indicates that their calculated polarization coefficient increases with flow rate. The membrane coefficient, C_m, is influenced by both the circulation rate and temperature with circulation rate having a pronounced effect as shown in Fig. 13c. At large circulation rates, the membrane coefficient grows with feed temperature while at lower flow rate it reverses its direction and decreases with inlet temperature. The results shown in Fig. 13 can be linked to the MD performance depicted in Fig. 8. For example, the enhanced mass flux with flow rates is not due to amplified driving force, as the bulk and membrane temperature differences are smaller at higher flow rates as shown in Figs. 7 and 13. In fact, as Fig. 13c indicates, the membrane permeability has the most effect on mass production when the flow rate is higher than 100 L/h. This means that a high circulation rate improves the hydrodynamics and, consequently, the transport mechanism through the porous membrane. In contrast, at a low flow rate, the membrane coefficient is very low and degrades with temperature, and the mass production is enhanced primarily by the temperature drop as evident in Figs. 13a and 7b. Nevertheless, the net mass production at low flow rates is insignificant compared to that at high flow rates, indicating that the membrane transport mechanism has a greater effect on mass flux than the temperature difference. In addition, Fig. 13d shows the calculated heat transfer coefficient at the membrane interface, which may reflect on the MD thermal behavior shown in Fig. 7. h_m is proportionally related to the membrane conductivity, which has a large value at a low flow rate, indicating high heat loss by conduction. Therefore, the exiting permeate is not sufficiently warmed up as illustrated in Fig. 7a. When the feed flow rate is high, the membrane conductivity converges to a minimum value that is invariant with feed temperature or feed flow rate. In this case, the heat transfer resistance by conduction reaches a minimum inevitable magnitude, allowing the permeate temperature to achieve the maximum attainable quantity. It should be noted, however, that the calculated process properties, such as h_m, TPC and C_m, may not follow standard behavior because the porosity is varying with operating conditions.

6. Conclusion

In this study, a fully equipped experimental setup for saline water desalination using direct contact membrane distillation is used. The study analyzes the process performance in terms of heat and mass flux over a wide range of operating conditions. The mass flux is manifested by distillate production and the heat flux by the membrane end temperatures. The analysis is based on variable flow rate and inlet temperature of the hot (saline) stream. It is found that at high flow rates specifically higher than 100 L/h, the heat flux reaches its upper limit as the exit permeate

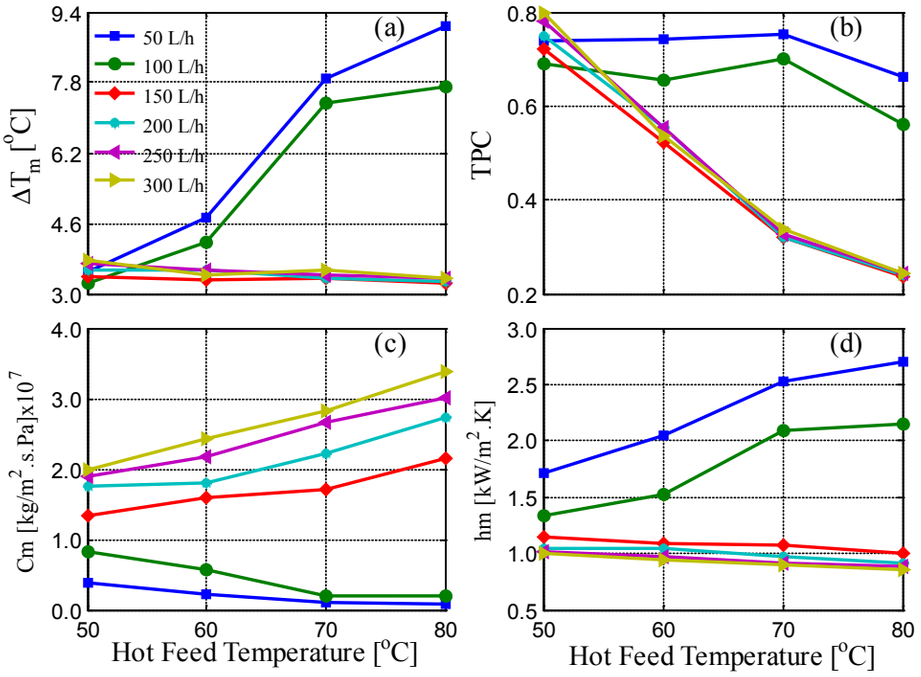

Fig. 13. Membrane interface characteristics, , salinity = 0.05%.

temperature reaches a maximum value that cannot be further exceeded. The experimental results include the effect of salinity on MD performance. An average flux decline of 12% is observed when the salinity is increased from 0.06% to 1%.

In addition, a theoretical model based on mass and energy balances has been calibrated and used in this work. Comparing the results of such a model with experimental data reveals its limitation in accurately tracking the physical process behavior over a wide range of operating conditions. Careful adjustment of the mass transfer coefficient and the heat losses improves the model accuracy in predicting the data. The experimentally calibrated model has been used to find acceptable values of the membrane properties, such as porosity and permeability, as well as the temperature polarization factor.

Acknowledgement

The project was supported by King Saud University, Deanship of Scientific Research, College of Engineering Research Center. The authors thank the Deanship of Scientific Research and RSSU at King Saud University for their technical support

Symbols

A_s — Surface area, m²
A — Cross sectional area, m²
a_i — Model calibration factor
C_m — Permeability coefficient, kg/m²s Pa
C_m^k — Knudsen mass flux coefficient, kg/m²s Pa
C_m^d — Moléculaire diffusion mass flux coefficient, kg/m²s Pa
C_m^C — Transition mass flux coefficient, kg/m²s Pa
C_p — Heat capacity, J/kg K
H_v — Latent heat of vaporization, J/kg
f — Fraction of heat losses used for model calibration
GOR — Gained output ratio
h_f, h_p, h_m — Feed, permeate, and membrane heat transfer coefficient, W/m² K
J — Mass flux, kg/m² h
k_m — Membrane conductivity, W/m K
m_c, m_w — Permeate and distillate flow rate, respectively, m³/h
$m_{h_{in}}$, $m_{h_{out}}$ — Hot water inlet and outlet flow rate, respectively m³/h
M_w — Molecular weight of water, g/mole
P_1, P_2 — Vapor pressure at feed and permeate membrane surface, Pa
PD — Membrane pressure multiplied by diffusivity, Pam²/s
P_a — Entrapped air pressure, Pa
q_f, q_p — Heat transfer rate at feed and permeate sections, W/m²
q_m — Heat of evaporation and conduction, W/m²
q_t — Overall heat flux, W/m²
r — Pore size, m
R — Ideal gas constant, J/mole K
T_h, T_c — Feed (hot) and permeate (cold) bulk temperature, K

T_{mh}, T_{mc} — Feed and permeate membrane temperature, K
T_{ref} — Reference temperature, K
TPC — Temperature polarization coefficient
U — Overall heat transfer coefficient, W/m^{2}K
ε_m — Porosity
ε — Termination criteria
τ — Membrane tortuosity
δ — Membrane thickness, mm
ρ — Density, kg/m^3

References

[1] IDA, Desalination by the Numbers, International Desalination Association, http://idadesal.org/desalination-101/desalination-by-the-numbers, last visited 22-2-2017.
[2] N. Eckardt, E. Cominelli, M. Galbiati, C. Tonelli, The future of science: food and water for life, Plant Cell, 21(2) (2009) 368–372.
[3] M. Al Dayel, Geothermal resources in Saudi Arabia, Geothermics, 17 (1988) 465–476.
[4] S. Rehman, A. Shash, Geothermal resources of Saudi Arabia – Country Update Report, *Proceedings World Geothermal Congress* 2005, Antalya, Turkey, 24–29 April 2005.
[5] H.M. Hanan, M. Taleb, Barriers Hindering the Utilisation of Geothermal Resources in Saudi Arabia, *International Conference and Exhibition on Green Energy & Sustainability for Arid Regions & Mediterranean Countries*, Le Royal Hotel Amman, Jordan, November, 10–12, 2009.
[6] R.I.S. AlMudaiheem, S.O.A. AlYousef, T. Sharif, A.K.M. AmirulIslam, Performance evaluation of ten years operation experience of brackish water RO desalination in Manfouha plants, Riyadh, Desalination, 120 (1998) 115–120.
[7] M. Khayet, Membranes and theoretical modeling of membrane distillation: a review, Adv. Colloid Interface Sci., 164 (2011) 56–88.
[8] M. Khayet, T. Matsuura, Membrane Distillation: Principles and Application, Elsevier, Netherlands, 2011.
[9] A. Alkhudhiri, N. Darwish, N. Hilal, Membrane distillation: a comprehensive review, Desalination, 287 (2012) 2–18.
[10] A.M. Alklaibi, N. Lior, Membrane-distillation desalination: status and potential, Desalination, 171 (2005) 111–131.
[11] J. Orfi, N. Loussif, Modeling of a membrane distillation unit for desalination, In: Desalination: Methods Costs and Technology. I.A. Urbaneness, ed., Nova Science Publishers, NY, 2010, pp. 143–174.
[12] M.S. El-Bourawi, Z. Ding, R. Ma, M.A. Khayat, Framework for better understanding membrane distillation separation process, J. Membr. Sci., 285 (2006) 4–29.
[13] M. Khayet, Desalination by Membrane Distillation. In: Encyclopedia of Life Support Science (EOLSS), Water and Wastewater Treatment Technologies, 2010.
[14] J. Phattaranawik, R. Jiraratananon, Direct contact membrane distillation: effect of mass transfer on heat transfer, J. Membr. Sci., 188 (2001) 137–143.
[15] M. Mahdi, A. Shirazi, A. Kargari, A review on applications of membrane distillation (MD) process for wastewater treatment, J. Membr. Sci. Res., 1 (2015) 101–112.
[16] D.U. Lawal, A.E. Khalifa, Flux prediction in direct contact membrane distillation, Int. J. Mater. Mech. Manufact., 2(4) (2014) 302–308.
[17] K. Nakoa, A. Date, A. Akbarzadeh, A research on water desalination using membrane distillation, Desal. Water Treat., 56(10) (2015) 2618–2630.
[18] J. Lee, Y. Kim, W. Kim, L. Francis, G. Amy, N. Ghaffour, Performance modeling of direct contact membrane distillation (DCMD) seawater desalination process using a commercial composite membrane, J. Membr. Sci., 478 (2015) 85–95.
[19] R.P. Raut, K.S. Kulkarni, Desalination by membrane distillation, Int. J. Adv. Eng. Res. Stud., 1(3) (2012) 115–121.
[20] M. Safavi, T. Mohammadi, High-salinity water desalination using VMD, Chem. Eng. J., 149 (2009) 191–195.
[21] C-D. Ho, C-H. Huang, F-C. Tsai, W-T. Chen, Performance improvement on distillate flux of counter current-flow direct contact membrane distillation systems, Desalination, 338 (2014) 26–32.
[22] E. Drioli, A. Ali, F. Macedonio, Membrane distillation: recent developments and perspectives, Desalination, 356 (2015) 56–84.
[23] F. Macedonio, E. Drioli, Pressure-driven membrane operations and membrane distillation technology integration for water purification, Desalination, 223 (2008) 396–409.
[24] H.E.S. Fath, S.M. Elsherbiny, A.A. Hassan, M. Rommel, M. Wieghaus, J. Koschikowski, M.V. Atansever, PV and thermally driven small-scale, stand-alone solar desalination systems with very low maintenance needs, Desalination, 225 (2008) 58–69.
[25] J. Koschikowski, M. Wieghaus, M. Rommel, V.S. Ortin, B.J. Suarez, R.B. Rodríguez, Experimental investigations on solar driven stand-alone membrane distillation systems for remote areas, Desalination, 248 (2008) 125–131.
[26] T-C. Chen, C-D. Ho, Immediate assisted solar direct contact membrane distillation in saline water desalination, J. Membr. Sci., 358 (2010) 122–130.
[27] M. Khayet, Solar desalination by membrane distillation: dispersion in energy consumption analysis and water production costs (a review), Desalination, 308 (2013) 89–101.
[28] D. Winter, J. Koschikowski, M. Wieghaus, Desalination using membrane distillation: experimental studies on full scale spiral wound modules, J. Membr. Sci., 375 (2011) 104–112.
[29] S. Kalogirou, Seawater desalination using renewable energy sources, Progr. Energy Combust. Sci., 31 (2005) 242–281.
[30] O. Andrjesdóttir, C.L. Ong, M. Nabavi, S. Paredes, A.S.G. Khalil, M. Bruno, D. Poulikakos, An experimentally optimized model for heat and mass transfer in direct contact membrane distillation, Int. J. Heat Mass Transfer, 66 (2013) 855–867.
[31] A. Al-Aenzi, A.Q. Sharif, M.I. Sanduk, A.R. Khan, Experimental investigation of heat and mass transfer in tubular membrane distillation module for desalination, ISRN Chemical Engineering, (2012) 1–8.
[32] K. Fard, Y.M. Manawi, T. Rhadfi, K.A. Mahmoud, M. Khraisheh, F. Benyahia, Synoptic analysis of direct contact membrane distillation performance in Qatar: A case study, Desalination, 360 (2015) 97–107.
[33] E. Close, E. Sørensen, Modelling of direct contact membrane distillation for desalination, 20th*European Symposium on Computer Aided Process Engineering* – ESCAPE20, 6–9 June 2010, Italy.
[34] G. Guan, X. Yang, R. Wang, A.G. Fane, evaluation of heat utilization in membrane distillation desalination system integrated with heat recovery, Desalination, 366 (2015) 80–93.
[35] H. Geng, J. Wang, C. Zhang, P. Li, H. Chang, Highwater recovery of RO brine using multi-stage air gap membrane distillation, Desalination, 355 (2015) 178–185.
[36] L.M.L. Camacho, J. Dumée, J. Zhang, M. Li, J. Duke, S. Gomez, S. Gray, Advances in membrane distillation for water desalination and purification applications, Water, 5 (2013) 94–196.
[37] B.L. Pangarkar, M.G. Sane, M. Guddad, Reverse osmosis and membrane distillation for desalination of groundwater: a review, ISRN Materials Science, Volume 2011, Article ID 523124, 1–9.
[38] S.T. Bouguecha, S.E. Alya, M.H. Al-Beiruttya, M.M. Hamdia, A. Boubakrib, Solar driven DCMD: performance evaluation and thermal energy efficiency, Chem. Eng. Res. Design, 100 (2015) 331–340.
[39] Y.C. Tzahi, V.D. Adams, A.E. Childress, Experimental study of desalination using direct contact membrane distillation: a new approach to flux enhancement, J. Membr. Sci., 228 (2004) 5–16.
[40] J.H. Zhang, S. Gray, J.D. Li, Modelling heat and mass transfers in DCMD using compressible membranes, J. Membr. Sci., 387 (2012) 7–16.
[41] J. Zhang, Theoretical and Experimental Investigation of Membrane Distillation, Ph.D. Thesis, Victoria University, Australia, 2011.

[42] D. Winter, J. Koschikowski, S. Ripperger, Desalination using membrane distillation: Flux enhancement by feed water deaeration on spiral-wound modules, J. Membr. Sci., 423–424, 15 (2012) 215–224.
[43] D. Winter, J. Koschikowski, D. Düver, P. Hertel, U. Beuscher, Evaluation of MD process performance: effect of backing structures and membrane properties under different operating conditions, Desalination, 323 (2013) 120–133.
[44] G. Rao, R. Sage, S.R. Hiibel, A.E. Childress, Simplified flux prediction in direct contact membrane distillation using a membrane structural parameter, Desalination, 351 (2014) 151–162.
[45] T-C. Chen, C-D. Ho, H-M. Yeh, Theoretical modeling and experimental analysis of direct contact membrane distillation, J. Membr. Sci., 330(1–2) (2009) 279–287.
[46] V. Karanikola, A.F. Corral, H. Jiang, A.E. Sáez, R.G. Arnold, Effects of membrane structure and operational variables on membrane distillation performance, J. Membr. Sci., 524 (2017) 87–96.
[47] F. Eleiwi, N. Ghaffour, A.S. Alsaadi, L. Francis, T-M. Laleg-Kirati, Dynamic modeling and experimental validation for direct contact membrane distillation (DCMD) process, Desalination, 384 (2016) 1–11.
[48] F. Mahmoudia, G.M. Goodarzia, S. Dehghania, A. Akbarzadeha, Experimental and theoretical study of a lab scale permeate gap membrane distillation setup for desalination, Desalination, 419 (2017) 197–210.

Appendix

The governing equations of the transport phenomena in the membrane distillation unit are obtained by energy and mass balances on the hot and cold streams and within the membrane itself. A model is developed based on these main assumptions [17,48]:

Steady state conditions

Constant membrane properties such as thickness, tortuosity, porosity, and pore size

No heat loss to the environment

The total pressure difference across the membrane is zero, indicating no mass transfer by viscous flow

Permeate channels are fully filled with pure water

The mass flux (*J*) of vapor transfer through pores is given by

$$J = C_m\left(P_1 - P_2\right)\left(\frac{\frac{kg}{m^2}}{s}\right) \tag{A.1}$$

In Eq. (A.1), P_1 and P_2 are the partial pressures of water vapor estimated at the membrane surface temperatures T_{mh} and T_{mc}, respectively. The partial pressure can be calculated using the Antoine equation [13,16]:

$$P_1 = \exp\left(23.238 - \frac{3841}{T_{hm} - 45}\right)\left(1 - C_s\right)\left(1 - 0.5C_s - 10C_s^2\right) \tag{A.1a}$$

$$P_2 = \exp\left(23.238 - \frac{3841}{T_{cm} - 45}\right) \tag{A.1b}$$

C_m is the MD coefficient calculated from three correlations depending on the type of mass transfer regime:

Knudson flow mechanism:

$$C_m^k = \frac{2\varepsilon r}{3\tau\delta}\left(\frac{8M_w}{\pi RT}\right)^{1/2} \tag{A.2}$$

Molecular diffusion mechanism:

$$C_m^D = \frac{\varepsilon}{\tau\delta}\frac{PD}{P_a}\frac{M_w}{RT} \tag{A.3}$$

Knudsen-molecular diffusion transition mechanism:

$$C_m^C = \left[\frac{3}{2}\frac{\tau\delta}{\varepsilon r}\left(\frac{\pi RT}{8M_w}\right)^{1/2} + \frac{\tau\delta}{\varepsilon}\frac{P_a}{PD}\frac{RT}{M_w}\right]^{-1} \tag{A.4}$$

In Eqs. (A.2)–(A.4), T is the average temperature at the membrane interface and can be approximated by:

$$T = \frac{T_{mh} + T_{mc}}{2} \tag{A.4a}$$

These different regimes depend on the wall collision theory of water molecules, and each regime dominates at a specific range of values for the mean free path of a water molecule. The heat transfer process occurs in three steps:

Convection from the feed bulk to the vapor–liquid interface at the membrane surface:

$$q_f = h_f\left(T_h - T_{mh}\right) \tag{A.5}$$

Convection from the vapor–liquid interface at the membrane surface to the permeate side:

$$q_p = h_p\left(T_{mc} - T_c\right) \tag{A.6}$$

where h_f and h_p denote the heat transfer coefficients on the feed and cold stream sides, respectively.

Evaporation and conduction through the microporous membrane:

$$q_m = JH_v + h_m\left(T_{mh} - T_{mc}\right) \tag{A.7}$$

where H_v is the water latent heat,which can be estimated using Eq. (A.7a) [32]; whereas, h_m is the conductive heat transfer coefficient and is equal to k_m/δ, where k_m and δ denote the membrane thermal conductivity and its thickness, respectively.

$$H_v(T) = 1850.7 + 2.8273\mathrm{T} - 1.6\times10^{-3}T^2 \tag{A.7a}$$

The heat transfer coefficient for the permeate and hot sides is calculated using a correlation for the Nusselt number appropriate for laminar flow [9]:

$$Nu = 0.298\,\mathrm{Re}^{0.646}\,\mathrm{Pr}^{0.316} \tag{A.7b}$$

where Re is Reynolds number and Pr is Prandtl number.

The total heat flux across the membrane is directly proportional to the bulk temperature difference and can be expressed as follows:

$$q_t = U(T_h - T_c) \tag{A.8}$$

For counter current flow, the bulk temperatures are taken as $T_h = T_{h_{in}}$ and $T_c = T_{c_{out}}$.

The overall heat transfer coefficient is given by

$$U = \left[\frac{1}{h_f} + \frac{1}{h_m + \frac{JH_v}{T_{mh} - T_{mc}}} + \frac{1}{h_p}\right]^{-1} \tag{A.9}$$

Understeady-state operation, the heat transfer in the three individual parts of the system reaches equilibrium:

$$q_f = q_m = q_p \tag{A.10}$$

Considering the macroscopic scale of the MD unit (Fig. A.1), the heat balance around the permeate side is given by Zhang [41]:

$$UA_s\left(T_h - T_c\right) = m_c\mathrm{c_p}\left(\mathrm{T_{c_{out}}} - \mathrm{T_{c_{in}}}\right) \tag{A.11}$$

where m_c and C_p denote the volume flow rate and specific heat at a constant pressure, respectively. Eq. (A.11) is used to compute the permeate exit temperature, Similarly, assuming a constant density and heat capacity,the mass and heat balance around the feed side is given by

$$UA_s\left(T_h - T_c\right) = m_{h_{in}}\mathrm{c_p}\left(\mathrm{T_{h_{out}}} - \mathrm{T_{ref}}\right) - m_{h_{out}}\mathrm{c_p}\left(\mathrm{T_{h_{in}}} - \mathrm{T_{ref}}\right) \tag{A.12}$$

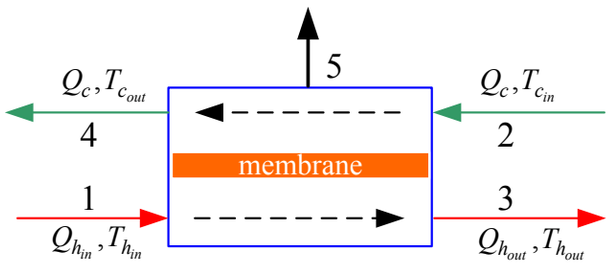

Fig. A.1. Typical DCMD unit.

$$m_{hin} - m_{h_{out}} = m_w \tag{A.13}$$

Eq. (A.12) is used for computing . It should be noted in Eqs. (A.11) and (A.12) that the heat losses are ignored. The temperature polarization coefficient is defined as follows:

$$TPC = \frac{T_{mh} - T_{mc}}{T_h - T_c} \tag{A.14}$$

The definitions of various variables, the numerical values of physical and design parameters in Eqs. (A.1)–(A.13), and additional supporting correlations are provided in various references [20–26].